Electronic Supplementary Information

Hierarchical Heterosturcture of SnO_2 Confined on CuS Nanosheets for Efficient Electrocatalytic CO_2 Reduction

Xiang Wang,[a] Jing Lv,[a] Jiaxu Zhang,[a] Xiao-li Wang,[a] Chaozhuang Xue,[a] Guoqing Bian,[a] Dongsheng Li,[b] Ying Wang[c] and Tao Wu[a,]*

[a] College of Chemistry, Chemical Engineering and Materials Science, Soochow University, Suzhou, Jiangsu 215123, China.

[b] College of Materials and Chemical Engineering, Hubei Provincial Collaborative Innovation Center for New Energy Microgrid, Key Laboratory of Inorganic Nonmetallic Crystalline and Energy Conversion Materials, China Three Gorges University, Yichang, Hubei 443002, China.

[c] Testing & Analysis Center, Soochow University, Suzhou, Jiangsu 215123, China.

*Corresponding author E-mail: wutao@suda.edu.cn

Product analysis

To determine the reduction products and their Faradaic efficiency (FE), electrolysis was conducted at selected potentials for 1 h in CO_2 saturated electrolyte under high stirring. Gas products in the headspace of the cathodic compartment were periodically (every 15 min) directly vented into the gas-sampling loop of a gas chromatograph (GC, Aligent 7890B). The distance of the gas circuit between the H-cell and the GC was kept as close as possible. The GC was equipped with a PLOT molecular sieve 5A and two Porapak Q columns. Nitrogen was used as the carrier gas. Reduction products were first analyzed by a thermal conductivity detector (TCD) for H_2 concentration, and then analyzed by flame ionization detector (FID) with a methanizer for CO and hydrocarbons. The concentration of gas products was quantified by integrating the peak area of the reduction products and determined from its standard calibration curve. Their Faradaic efficiency was calculated as follows:

$$\mathrm{FE}\ (\%) = \frac{Q_{gas}}{Q_{tot}} \times 100\% = \frac{n \times N \times F}{I \times t} \times 100\% = \frac{(\frac{P \times V_{loop} \times x}{R \times T}) \times N \times F}{I \times (\frac{V_{loop}}{\nu} \times 60\ \mathrm{s/min})} \times 100\% \quad (1)$$

where n is number of moles of CO or H_2, $N = 2$ is the number of electrons required to form a molecule of CO or H_2, F is the Faraday constant (96,500 C/mol), I is the recorded current, P = 101325 Pa is the standard atmospheric pressure, V_{loop} = 1 mL is the volume of sample loop of GC, R = 8.314, T = 298.15 K, x is the measured concentration of product based on the calibration of the GC with a standard gas.

The liquid product was collected at the end of each electrocatalysis, identified to only contain formate by a nuclear magnetic resonance (NMR) spectrometer (Aligent DirectDrive2, 600 MHz). Solvent pre-saturation technique was implemented to suppress the water peak. 500 μL electrolyte was mixed with 100 μL D_2O and 50 μL dimethyl sulfoxide (DMSO) stand solution, where DMSO was used as an internal standard to quantify the liquid product. To prepare the DMSO stand solution, 50 μL pure DMSO (Sigma, 99.99%) was diluted to 1000 mL with Milli-Q water. The FE of formate was calculated as follows:

$$FE_{HCOO^-}(\%) = \frac{Q_{HCOO^-}}{Q_{tot}} \times 100\% = \frac{n_{HCOO^-} \times N \times F}{I \times t} \times 100\% \quad (2)$$

where n_{HCOO^-} is the measured amount of formate in the cathodic compartment, t is the electrolysis time, $N = 2$ is the number of transferred electrons for the formation of one formate molecule, F is the Faraday constant (96,500 C/mol), I is the current at the potential applied on the electrochemical system. The partial current density of each product at different potentials was calculated by multiplying the overall geometric current density and its corresponding Faradaic efficiency.

Theoretical calculations

Adsorption energy ΔE of A groups on the surface of substrates was defined as:

$$\Delta E = E_{*A} - (E_* + E_A) \quad (3)$$

where *A and * denote the adsorption of A group on substrates and the bare substrates, E_A denotes the energy of A group.

The CO_2RR involving a $2e^-$ pathway can be described by:

$$CO_2\,(g) + (H^+ + e^-) + * \rightarrow OCHO^* + (H^+ + e^-) \rightarrow * + HCOOH\,(l) \quad (4)$$

$$CO_2\,(g) + (H^+ + e^-) + * \rightarrow COOH^* + (H^+ + e^-) \rightarrow CO^* + H_2O \rightarrow * + CO\,(g) \quad (5)$$

Where a lone asterisk (*) represents a vacant surface catalytic active site and * symbol after a molecule denotes intermediate species adsorbed on the active site, while OCHO*, COOH*, and CO* represent reaction intermediates, respectively. Free energy change ΔG of the reaction was calculated as the difference between the free energies of the initial and final states as shown below:[1]

$$\Delta G = \Delta E + \Delta E_{ZPE} - T\Delta S - eU \quad (6)$$

where the ΔE denotes the adsorption energy, ΔE_{ZPE} and ΔS are the changes of zero-point energy and entropy, and the temperature T is set to 300 K. U is the potential measured against normal hydrogen electrode (NHE) at standard conditions; e = 1 is the transferred charge for one electron reaction. Considering about the NHE, U = 0. ZPE and E were computed from the temperature, pressure, and vibrational energy via standard methods. For free energies of adsorbates, all 3N degrees of freedom were treated as harmonic vibrations and the contributions from the catalyst surfaces were neglected. The relevant contributions to G are listed in Table S5. Moreover, a series of gas-phase thermochemical reaction enthalpies were tested to correct the E_{DFT} of CO_2, CO, and $HCOO^-$, because of the inaccuracy of the PBE functional to describe the energy of the OCO-containing gas-phase species (a systematic error).[2] The effects of dipole correction for adsorbates were also included. The theoretical overpotential (U_{op}) can be deduced from the free energy difference between the equilibrium potential (U_0) and the calculated limiting (or onset) potential (U), $U_{op} = U_0 - U$.

Figure S1. Photographic image of as-synthesized SnO_2/CuS NSs dispersed in reaction medium.

The proposed synthetic mechanism is described simply as follow: when Na_4SnS_4 was dissolved in water, it experienced a slow hydrolysis process to simultaneously form SnO_2 nuclei and Na_2S species. Subsequently, $CuCl_2$ reacted with the preformed Na_2S to generate CuS nuclei. Over time, the previously formed small CuS nuclei gradually aggregated to grow into crystalline hexagonal NSs, which meanwhile afforded suitable substrate for the heterogeneous nucleation of SnO_2 NPs and promoted the formation of hierarchical SnO_2/CuS NSs according to the classical theory of nucleation and growth of NPs.[3]

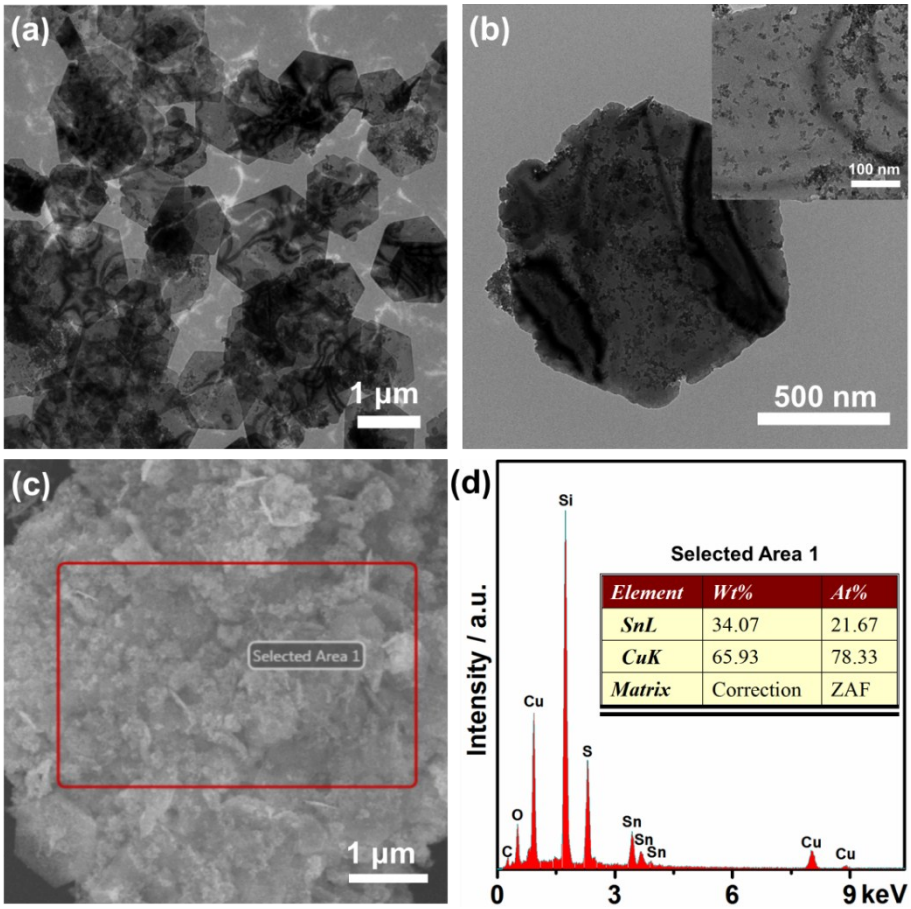

Figure S2. (a, b) Low-magnification TEM images and corresponding magnified image (inset of b), (c) SEM image and (d) corresponding EDS result of as-synthesized SnO_2/CuS NSs.

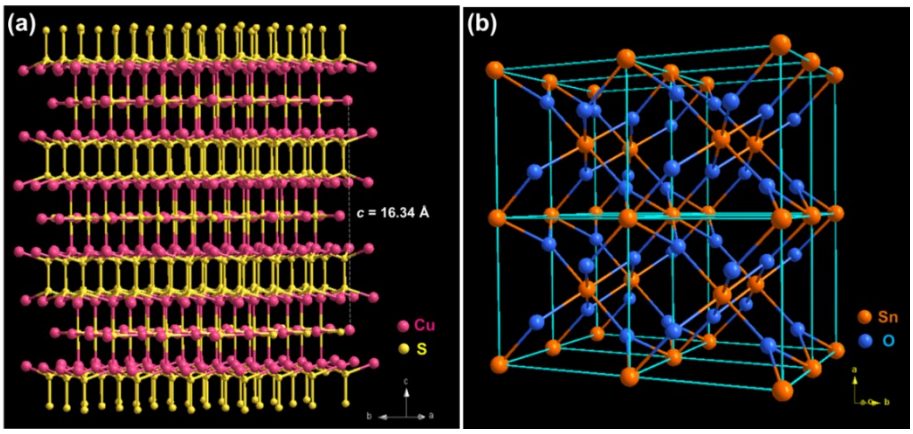

Figure S3. The spatial crystal structure model of CuS (a) and rutile SnO_2 supercell (2×2×2) (b). The covellite CuS crystal model consists of three alternating CuS_3-Cu_3S-CuS_3 layers and S-S layers along the *c* axis and the lattice constants of *c* is 16.34 Å, according to the standard PDF card # 78-0877.

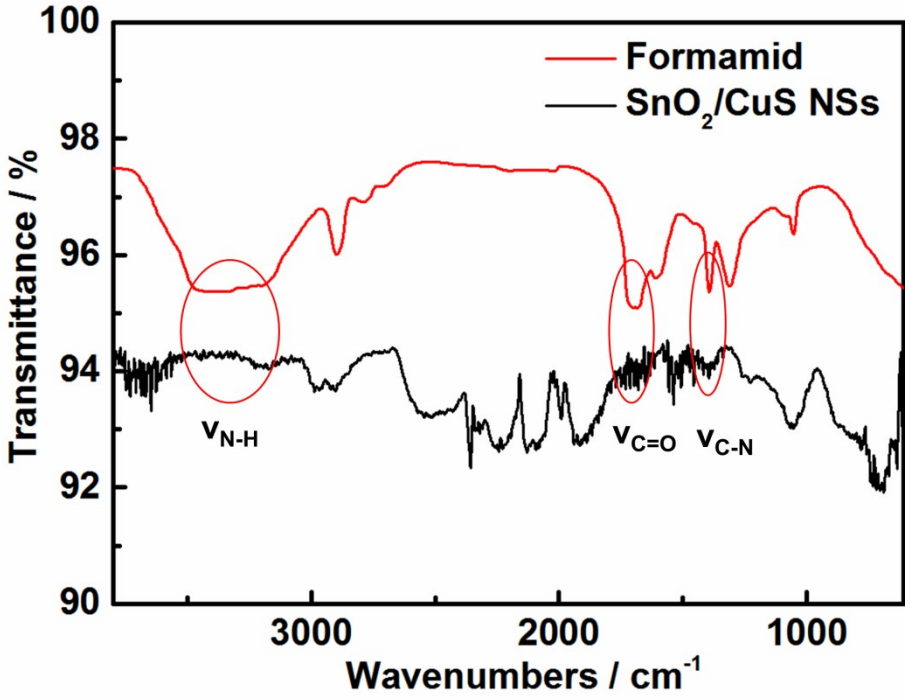

Figure S4. FTIR spectra of as-synthesized SnO_2/CuS NSs (black) and formamide (red). The IR band at 1390-1400 cm^{-1} is attributed to C-N vibrations, 1670-1720 cm^{-1} to C=O vibrations, 3220-3455 cm^{-1} to N-H vibrations, which are caused by the existence of organic amine.

To be noted, compared to CuS NSs capped by organic molecules synthesized through solvent-coordination-molecular-template-guided high-temperature wet-chemistry method,[4] the as-synthesized SnO_2/CuS NSs through this route are absence of the used organic amine solvent, which is convenient and favourable for catalytic applications as free of further energy-exhaustive post anneal to expose active sites.

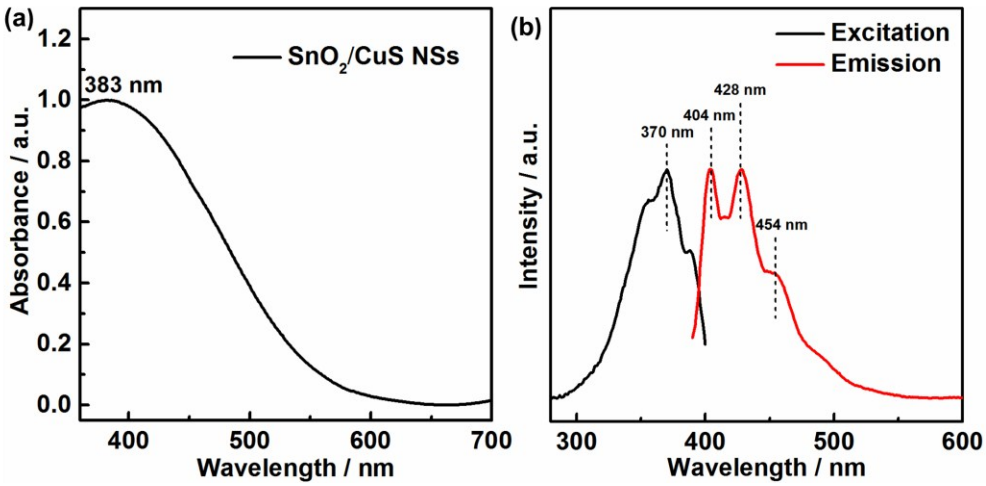

Figure S5. (a) UV-vis absorption spectrum and (b) room-temperature photoluminescence (PL) excitation and emission spectra of as-obtained ultrathin SnO_2/CuS NSs.

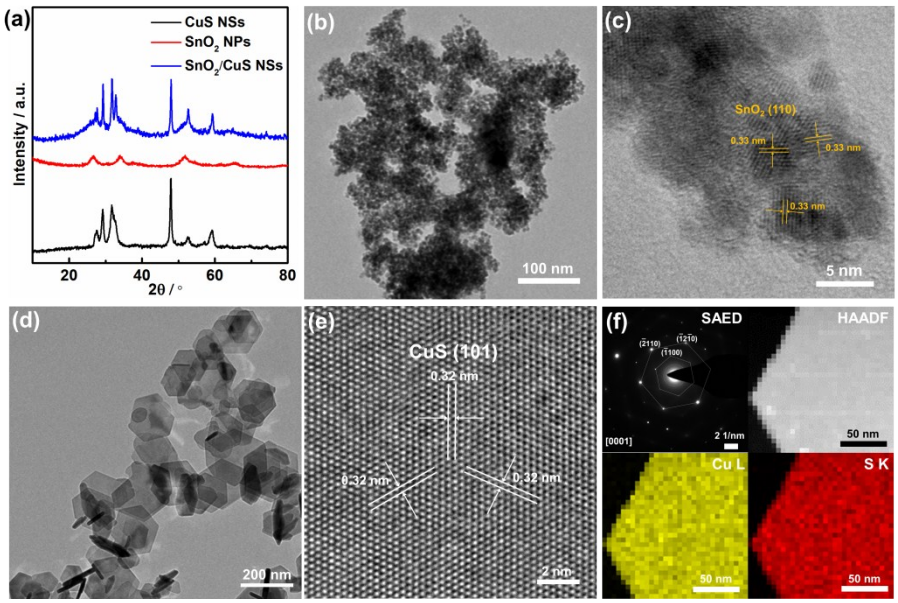

Figure S6. (a) XRD patterns of as-synthesized CuS NSs, SnO_2 NPs and SnO_2/CuS NSs; (b, d) TEM and (c, e) HRTEM images of as-synthesized SnO_2 NPs and CuS NSs, respectively; (f) SAED pattern and HAADF-STEM and corresponding elemental mapping images of CuS NSs.

To be noticed, the lateral size of as-synthesized pure CuS NSs was distinctly smaller than that of hierarchical CuS NSs (Figure S2), which is on account of fast generation of S^{2-} ions by Na_2S as the sulfur source, compared to the slow hydrolysis speed of Na_4SnS_4.

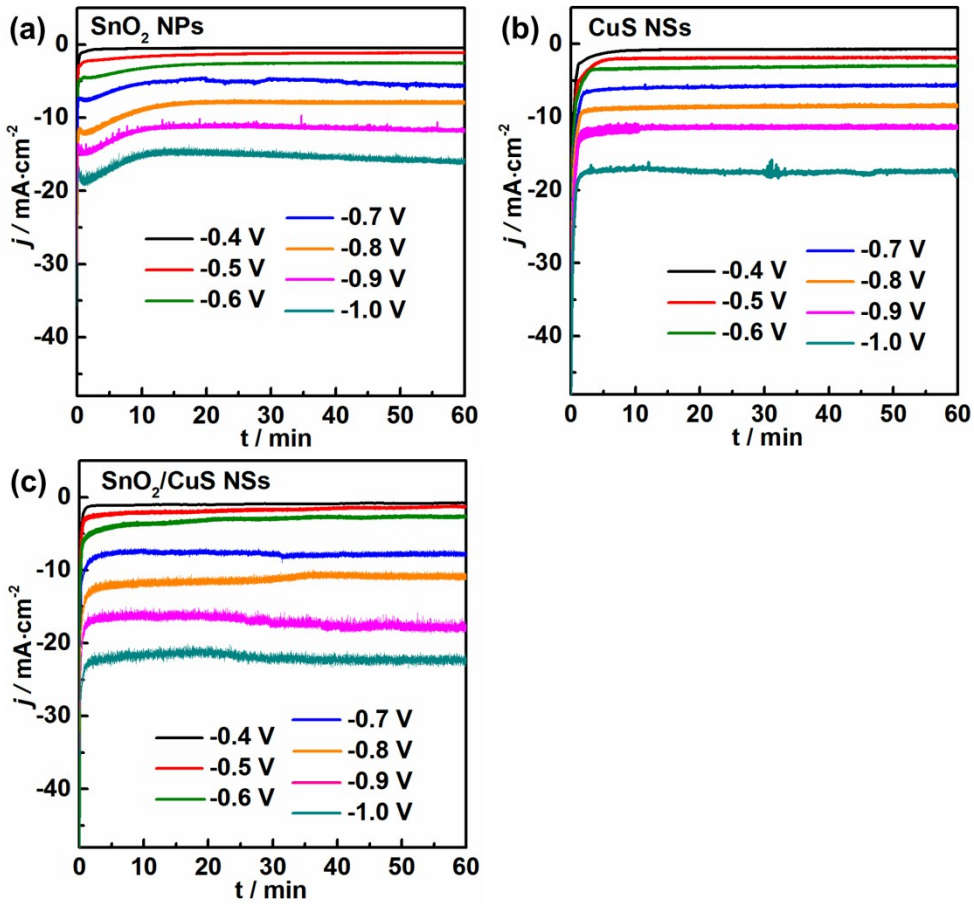

Figure S7. Potential-dependent chronoamperometry of (a) SnO_2 NPs, (b) CuS NSs and (c) SnO_2/CuS NSs for the electrochemical CO_2 reduction reaction

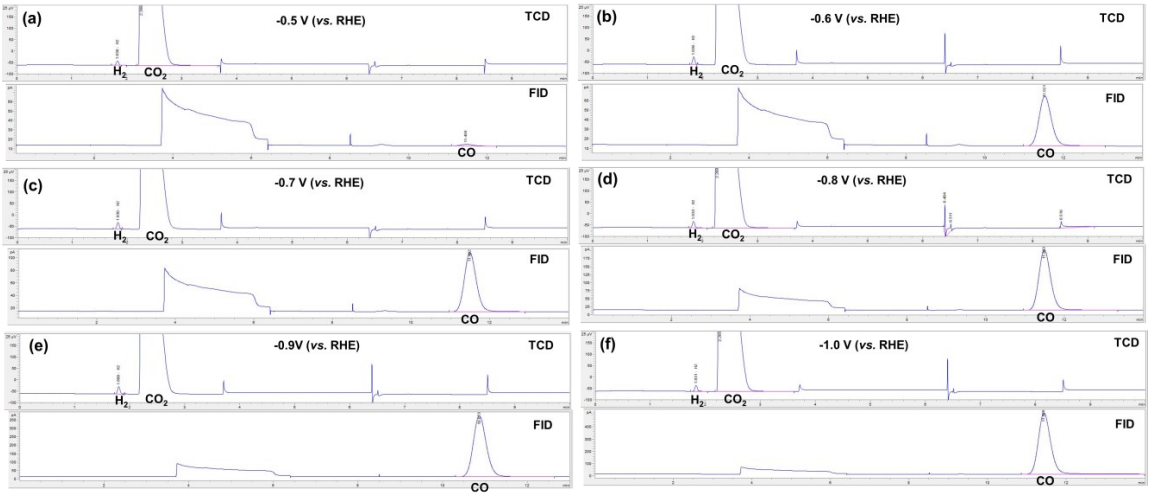

Figure S8. Gas chromatography (GC) spectra of gaseous products during the electrochemical CO_2 reduction processes at different potentials for the SnO_2/CuS (1:1) NSs. Some particularly narrow and sharp peaks in the spectra are attributed to the valves switch of GC.

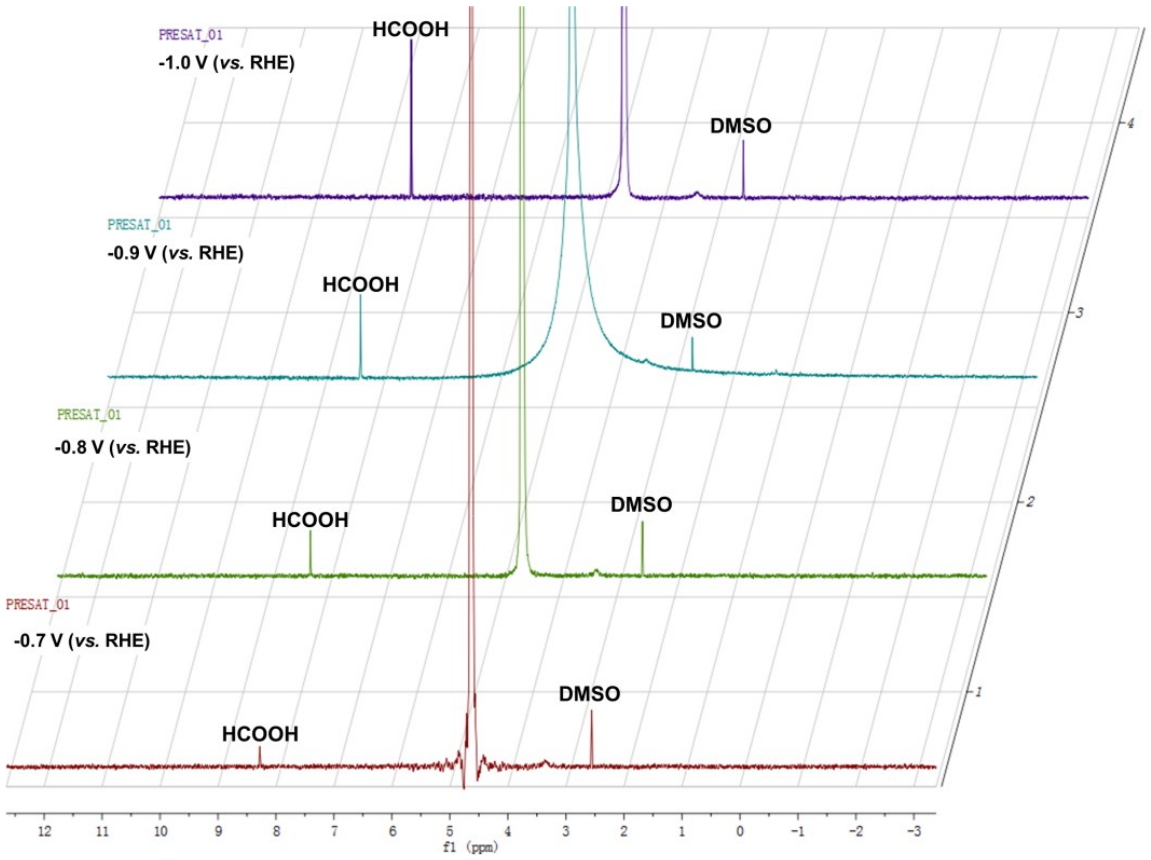

Figure S9. ^{1}H nuclear magnetic resonance (^{1}H-NMR) spectra of the electrolyte after electrochemical CO_2 reduction for the SnO_2/CuS NSs at different potential for one hour**.** DMSO (dimethyl sulphoxide) is used as an internal standard for quantification of liquid products.

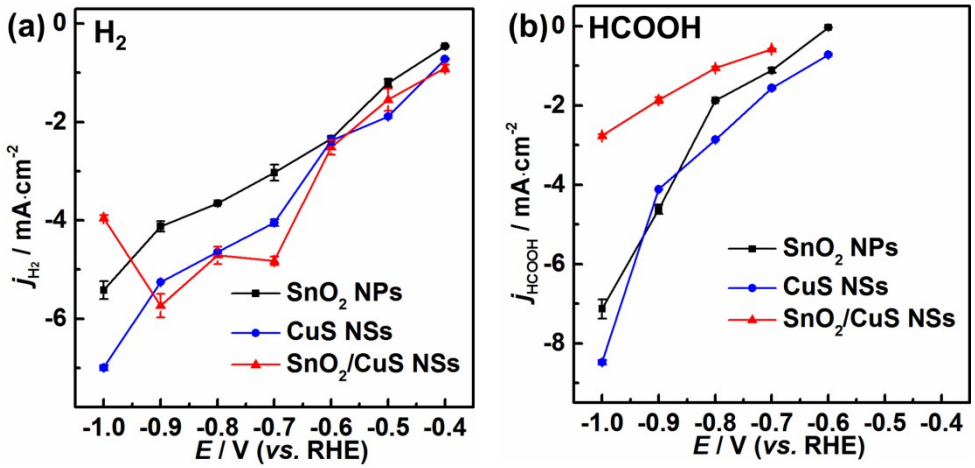

Figure S10. Potential-dependent (a) H_2 and (b) formate partial current densities for SnO_2 NPs, CuS NSs and SnO_2/CuS NSs catalysts.

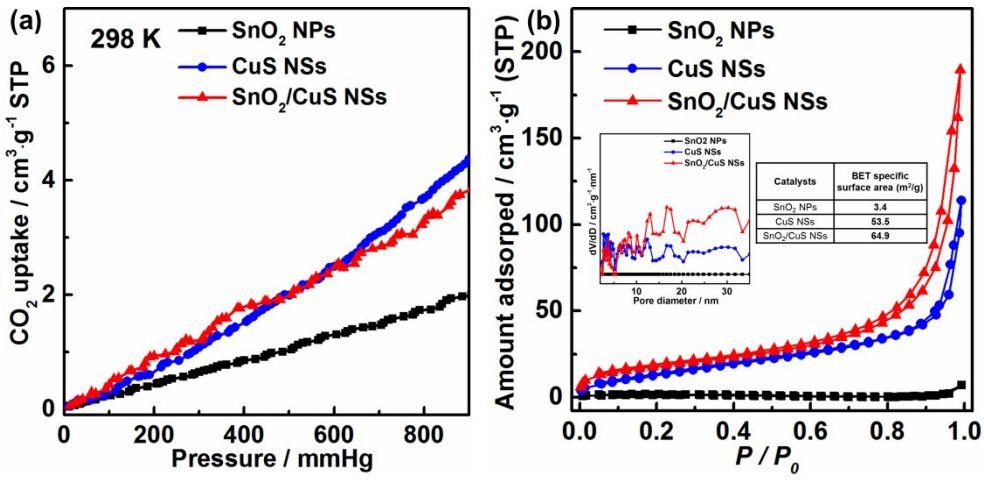

Figure S11. (a) CO_2 and (b) N_2 adsorption isotherms of various catalysts tested at 298 K and 77 K, respectively. Inset, pore size distributions and specific surface of each catalyst.

As shown in Figure S11b, SnO_2 NPs exhibited little N_2 adsorption and other samples showed type-II isotherms with H3 type hysteresis loops in the relative pressure range of 0 to 1, implying the presence of meso-slit pores.[5] And the Brunauer-Emmett-Teller (BET) specific surface area (SSA) of SnO_2 NPs, CuS NSs and SnO_2/CuS NSs are 3.4, 53.5 and 64.9 m^2/g, respectively. The increased BET SSA of hierarchical SnO_2/CuS NSs may be caused by SnO_2 NPs decorated on the surface of CuS NSs, which increased the SSA of slit pores formed by accumulation of CuS NSs, as the much more obvious H3 type hysteresis loop existed in SnO_2/CuS NSs than other samples. The Non-local Density Function Theory (NLDFT) pore size distributions estimated according to the adsorption branch of the nitrogen isotherms (inset of Figure S11b) also indicated a broad distribution in mesoporous range and increased pore volume of SnO_2/CuS NSs. The enlarged mesopores enable higher local concentration of CO_2 molecules in SnO_2/CuS NSs, which may be beneficial to CO_2 reduction.

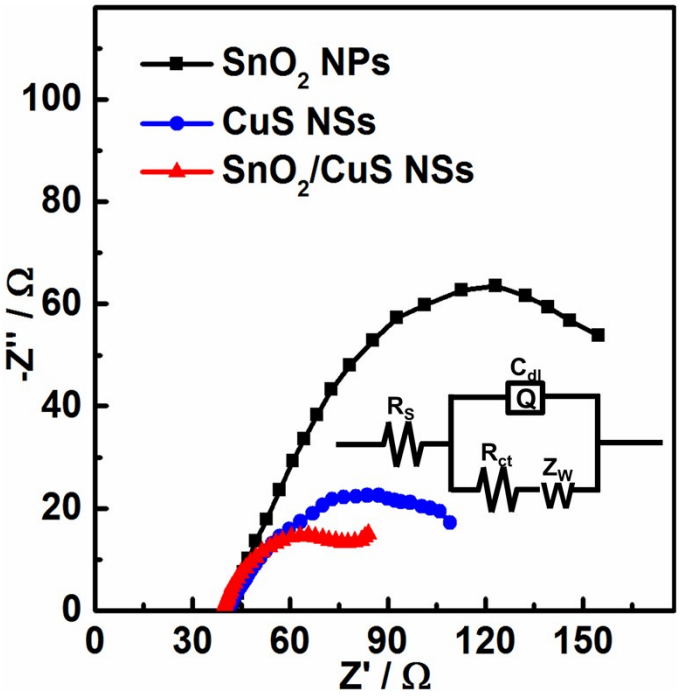

Figure S12. Nyquist plots for CuS NSs, SnO_2 NPs and SnO_2/CuS NSs, respectively. Inset of is the electrical equivalent circuit: R_S is the solution resistance, C_{dl} is the double layer capacitance, R_{ct} is the electron transfer resistance and Z_W is the Warburg-type impedance.

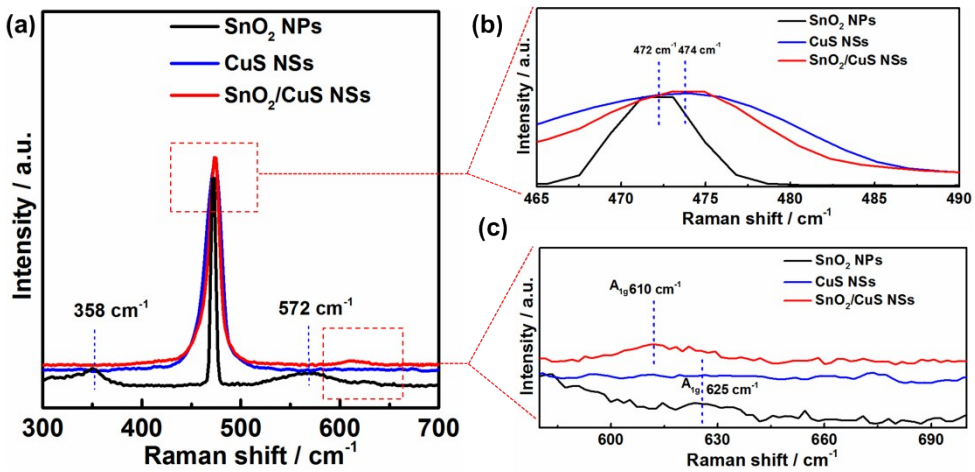

Figure S13. Raman spectra of SnO_2 NPs, CuS NSs, SnO_2/CuS NSs, and the mixture of CuS NSs and SnO_2 NPs.

As shown in Figure S13a, two peaks of 358 and 572 cm^{-1} could only be observed in SnO_2 NPs, implying the small grain size of SnO_2 NPs.[6] Meanwhile, the peaks at 358 and 572 cm^{-1} for SnO_2 NPs, belonging to the surface phonon modes caused by surface phonons scattering, disappeared in CuS/SnO_2 NSs, owing to the decoration of SnO_2 NPs on the surface of CuS NSs.[7] On the other hand, the A_{1g} vibration mode of SnO_2 at 610 cm^{-1} for SnO_2/CuS NSs (Figure S13c), originating from interior phonons scattering, red shifted about 15 cm^{-1} compared to the pure SnO_2 NPs,[6] implying the weakened force constant and thus increased interatomic distances in the interior of SnO_2 NP_S of SnO_2/CuS NSs.[6] This phenomenon is probably due to the interaction between of SnO_2 NPs and CuS NSs, where the matched interplanar lattice fringe spacing existed as displayed in HRTEM image (Figure 1d).

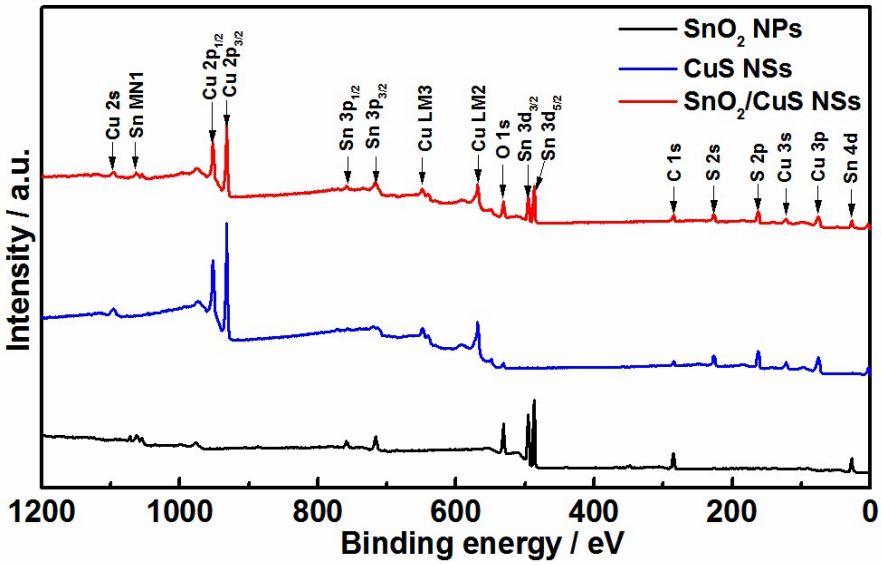

Figure S14. XPS survey spectra of as-synthesized SnO_2 NPs (black), CuS NSs (red), SnO_2/CuS NSs (blue).

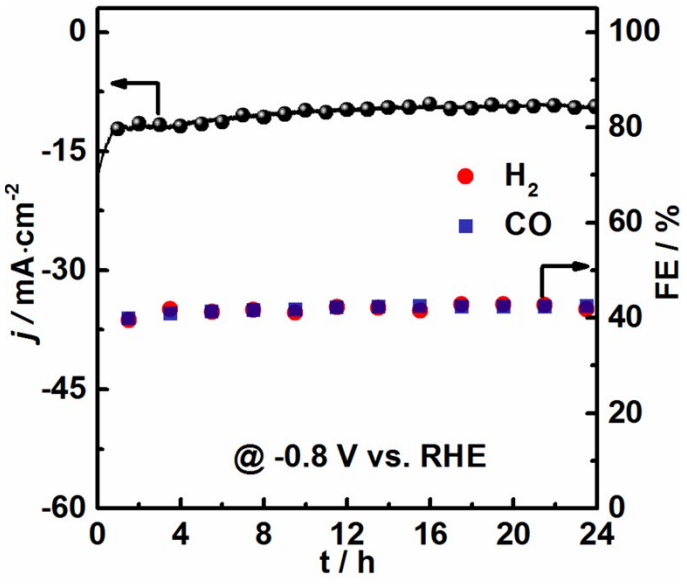

Figure S15. Chronoamperometry and corresponding FE_{H2} and FE_{CO} results of SnO_2/CuS NSs at -0.8 V versus RHE for 24 h.

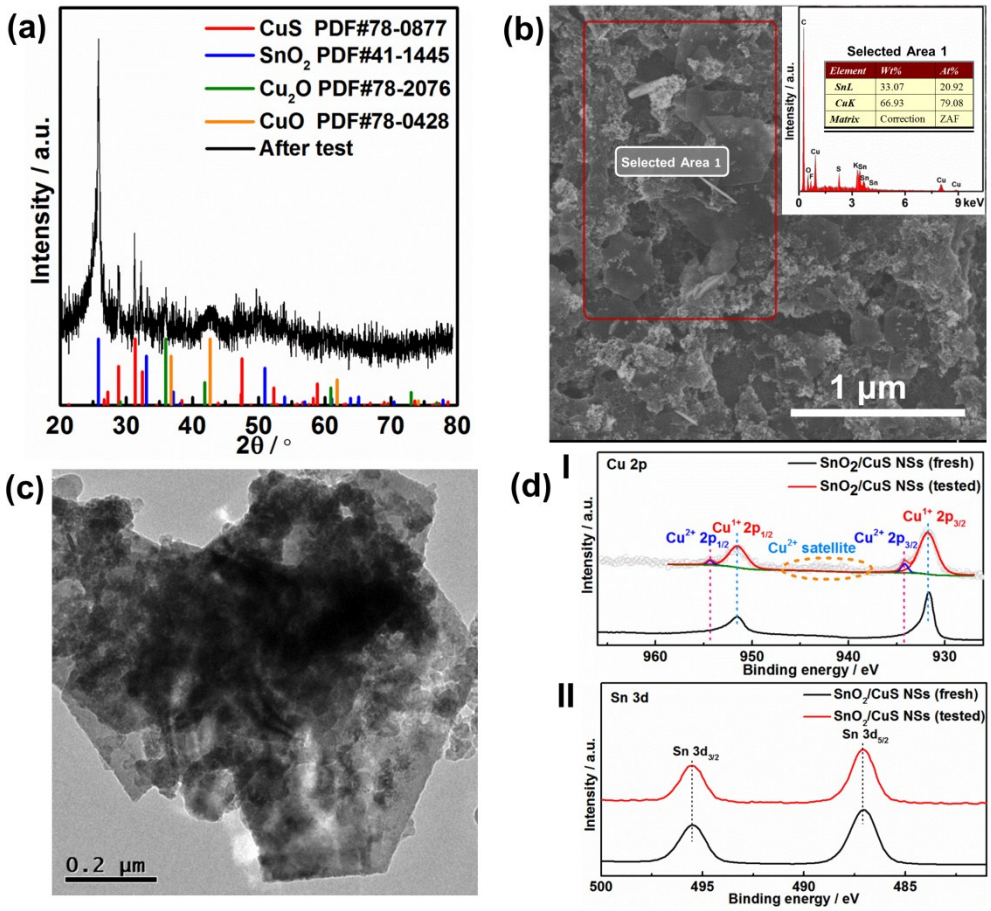

Figure S16. (a) XRD pattern, (b) SEM image and corresponding EDS result, (c) TEM image and (d) high-resolution XPS spectra of (I) Cu 2p and (II) Sn 3d auger spectra of SnO_2/CuS NSs after 24 h stability test for electrochemical CO_2RR at at -0.8 V versus RHE.

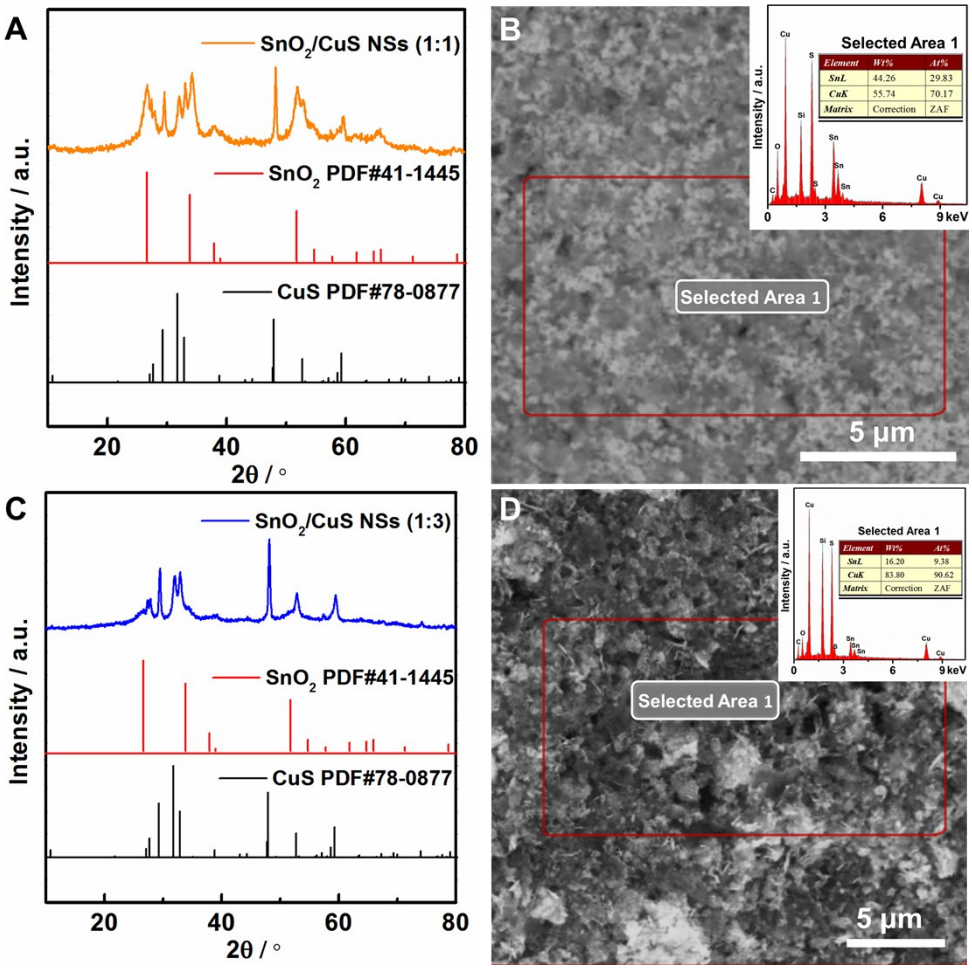

Figure S17. (a, c) XRD patterns and (b, d) SEM images and corresponding EDS result of as-synthesized SnO_2/CuS (1:1), SnO_2/CuS (1:3) samples, respectively. (inset of b and c, corresponding magnified images).

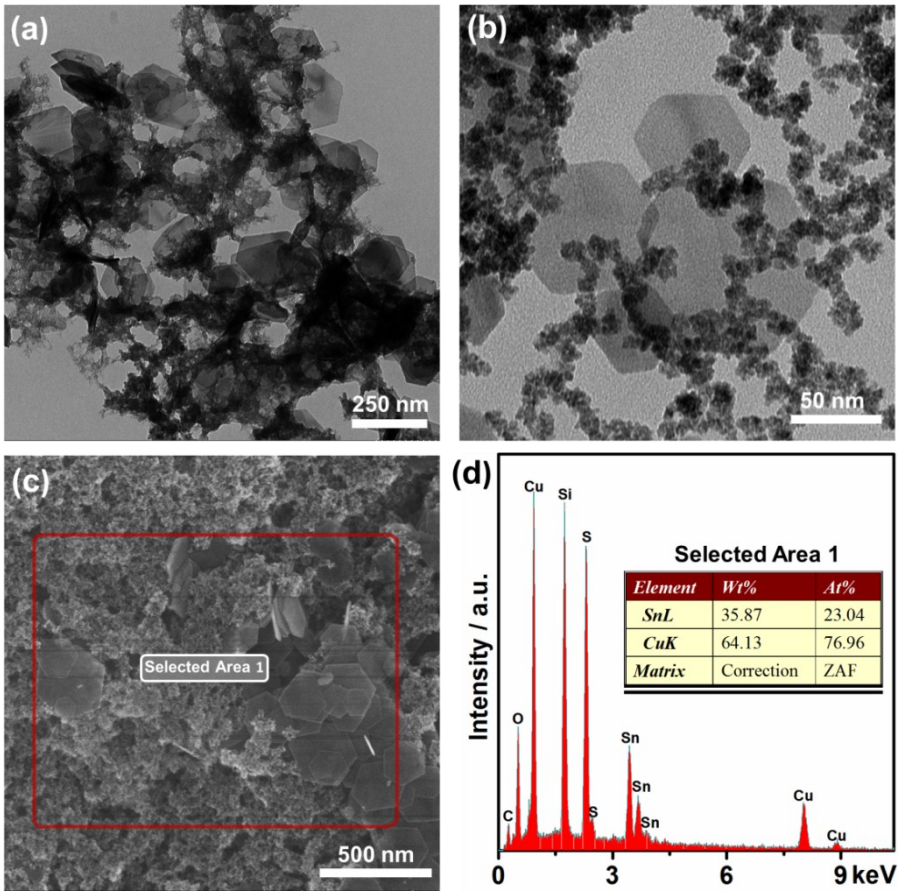

Figure S18. (a), (b) TEM images, (c) SEM image and (d) corresponding EDS result of physical mixture of SnO_2 NPs and CuS NSs (SnO_2 NPs + CuS NSs).

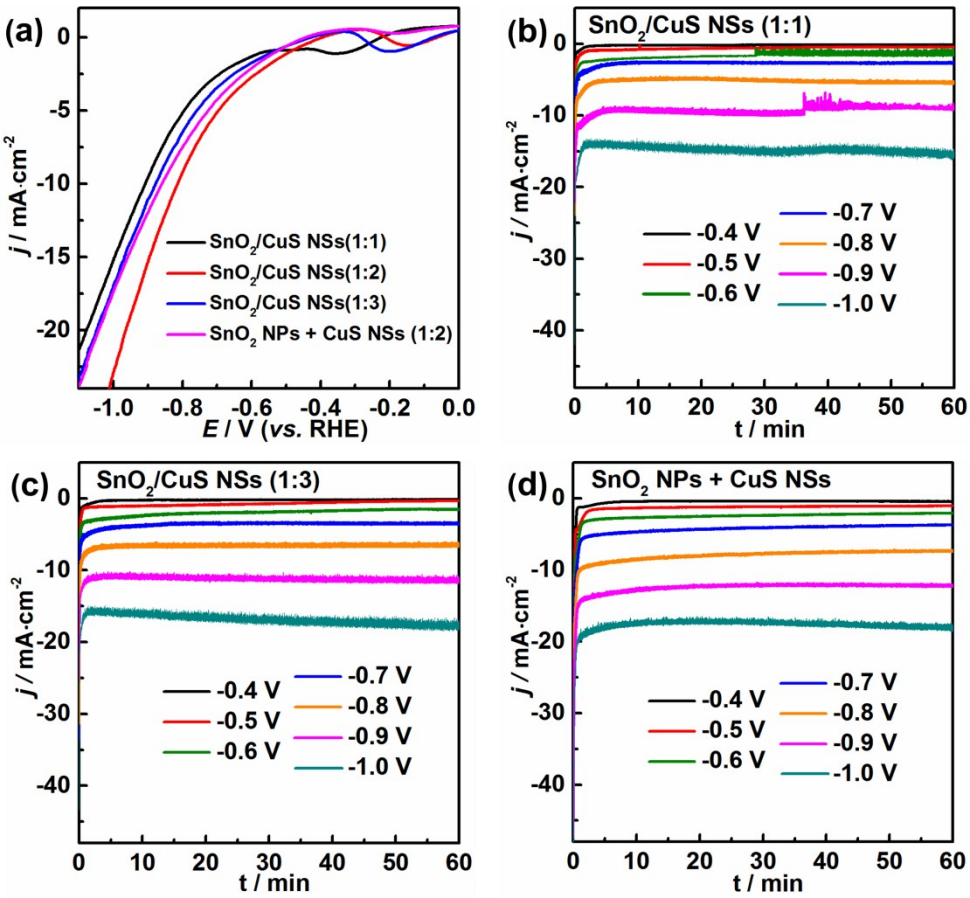

Figure S19. (a) Linear sweep voltammetry (LSV) curves of SnO_2/CuS NSs (1:1), (1:2), (1:3) and mixture of SnO_2 NPs and CuS NSs catalysts in CO_2-saturated 0.1 M $KHCO_3$ aqueous solution, scan rate = 5 mV/s. Potential-dependent chronoamperometry of (b) SnO_2/CuS NSs (1:1), (c) (1:3) and (d) physical mixture of SnO_2 NPs and CuS NSs catalysts for the electrochemical CO_2 reduction reaction.

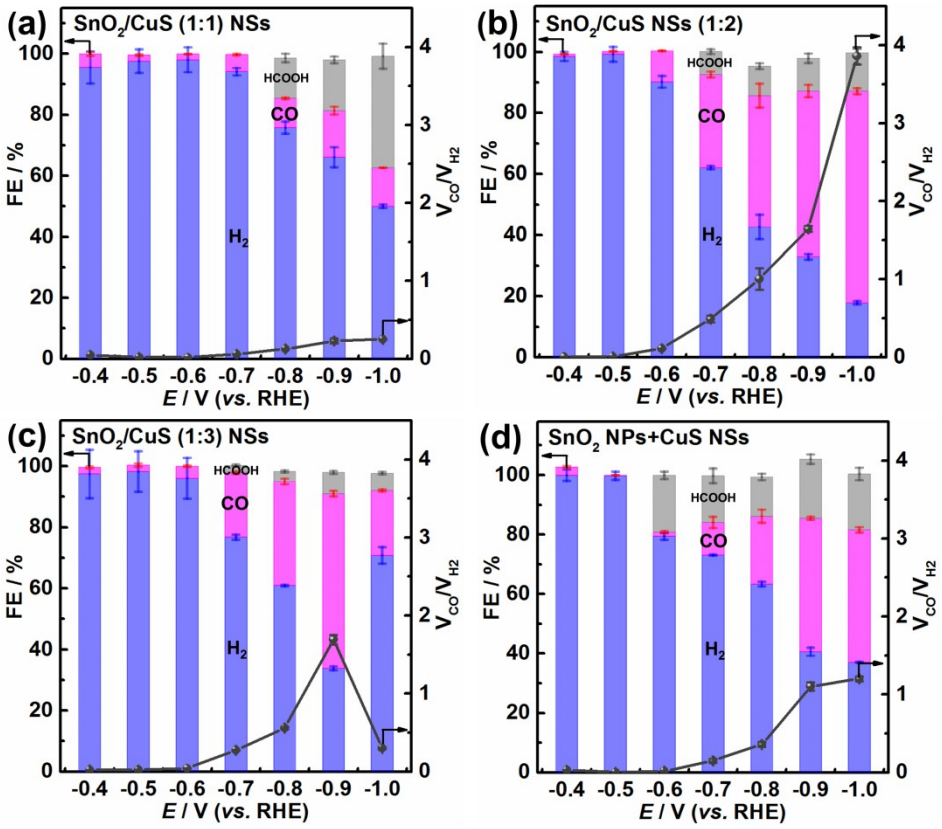

Figure S20. Faradaic efficiency and CO/H_2 ratio for electrochemical reduction of CO_2 measured on (a) SnO_2/CuS (1:1) NSs, (b) SnO_2/CuS (1:2) NSs, (c) SnO_2/CuS (1:3) NSs and (d) physical mixture of SnO_2 NPs and CuS NSs.

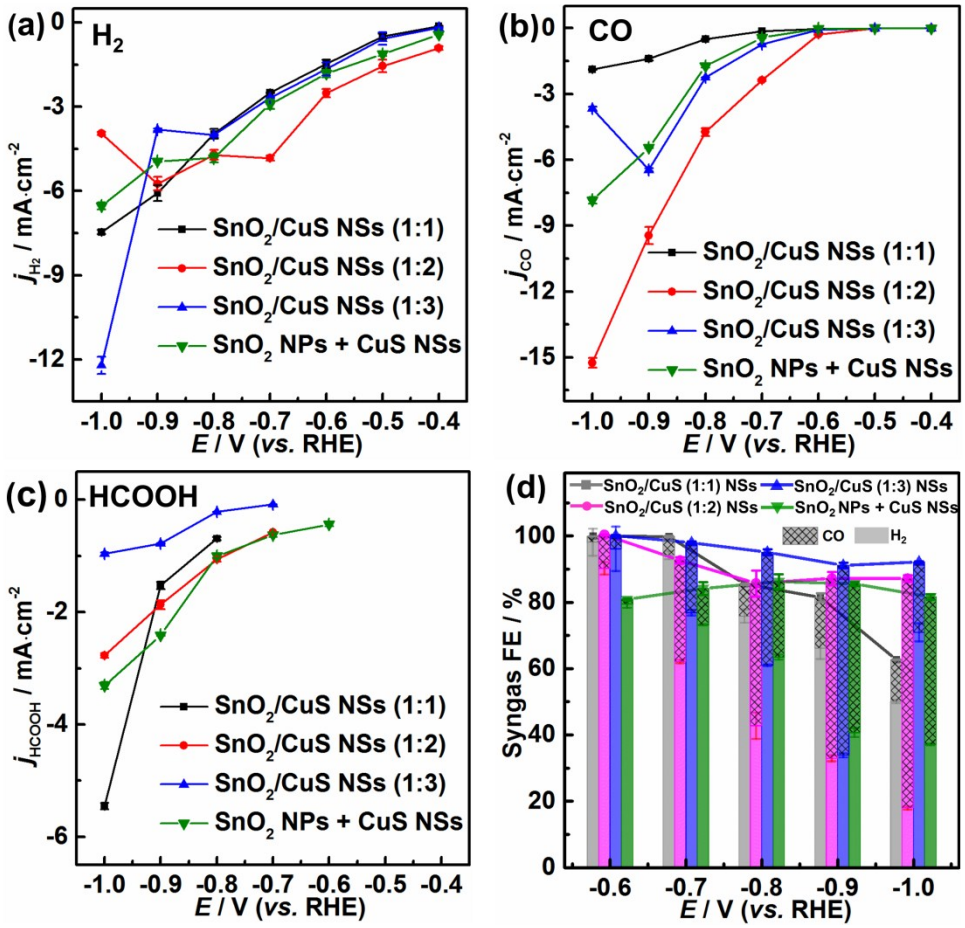

Figure S21. Potential-dependent (a) H_2, (b) CO and (d) formate partial current densities and (d) Faradaic efficiencies (FE) of syngas (CO + H_2) for SnO_2/CuS (1:1) NSs, SnO_2/CuS (1:2) NSs, SnO_2/CuS (1:3) NSs and physical mixture of SnO_2 NPs and CuS NSs.

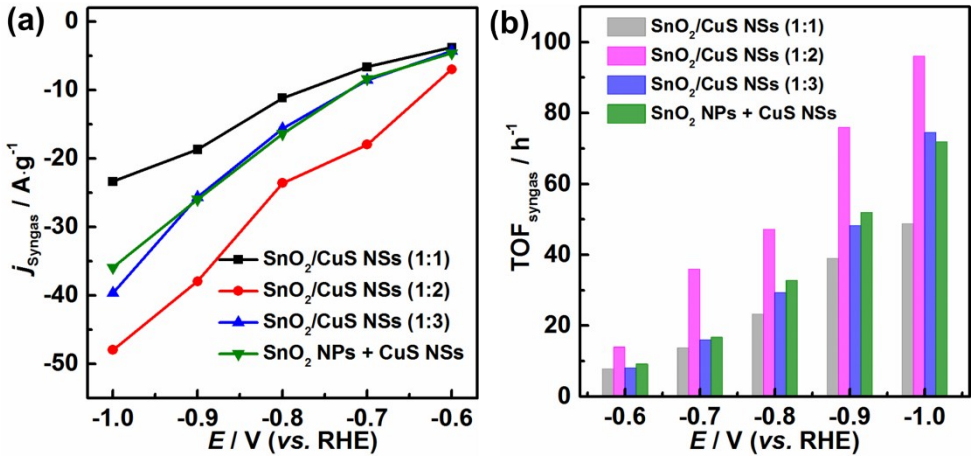

Figure S22. (a) The mass activity (current per catalyst mass) and (b) TOFs of syngas ($CO+H_2$) for SnO_2/CuS NSs (1:1), SnO_2/CuS NSs (1:2), SnO_2/CuS NSs (1:3) and physical mixture of SnO_2 NPs and CuS NSs.

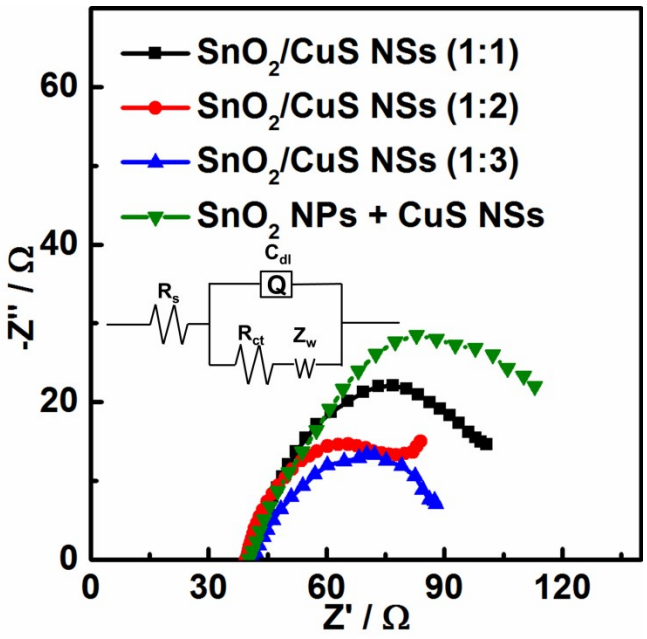

Figure S23. Nyquist plots for SnO_2/CuS NSs (1:1), SnO_2/CuS NSs (1:2), SnO_2/CuS NSs (1:3) and physical mixture of SnO_2 NPs and CuS NSs. Inset is the electrical equivalent circuit.

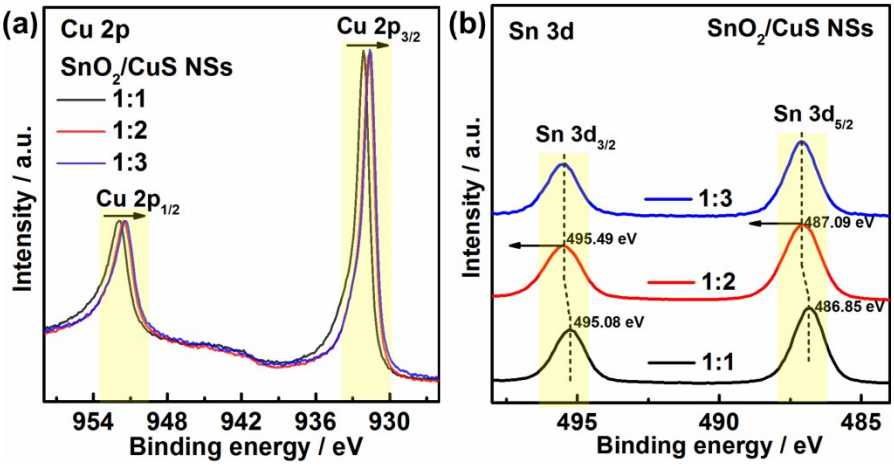

Figure S24. Comparison of high resolution XPS spectra of (a) Cu 2p, (b) Sn 3d spectra of as-synthesized different ratio of SnO_2/CuS NSs samples.

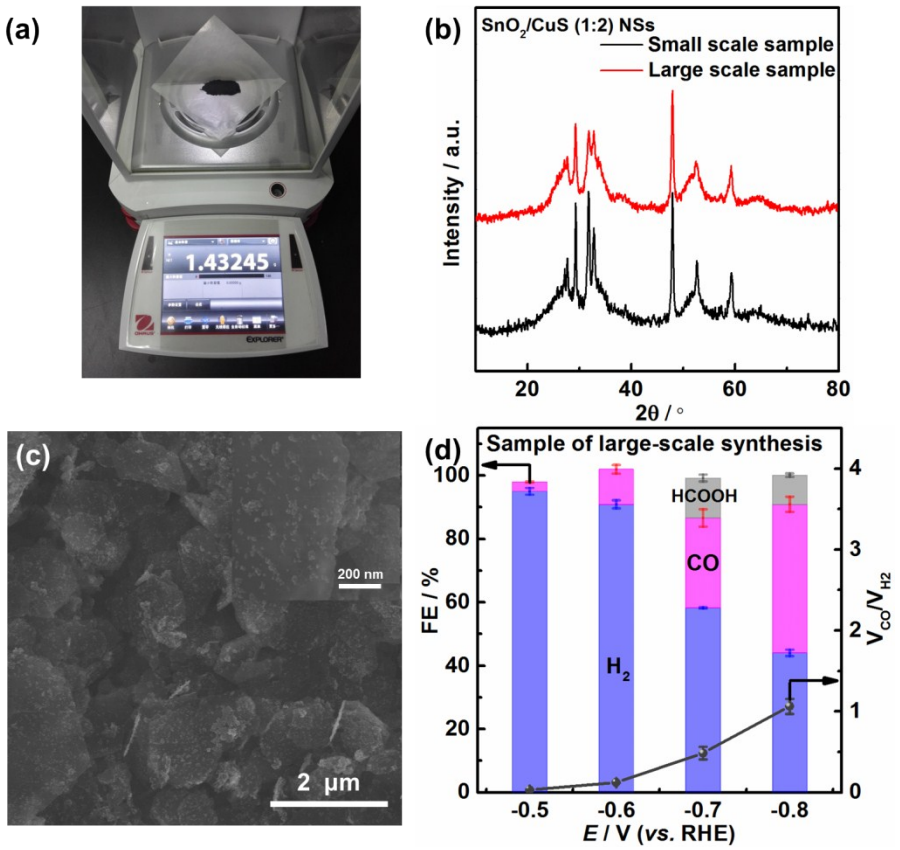

Figure S25. (a) Photographic image of hierarchical SnO_2/CuS nanosheets synthesized in a large amount of ~ 1.4 g; (b) XRD patterns, (c) SEM image and (d) FE of electrochemical reduction of CO_2 of hierarchical SnO_2/CuS NSs synthesized in a large amount. This synthetic strategy can be easily reproduced and scaled up. For example, to demonstrate the large-scale synthesis, we performed the reaction with 15 mmol of $CuCl_2$ precursor and obtained as much as ~ 1.4 g of hierarchical SnO_2/CuS nanosheets without a size-sorting process.

Figure S26. Photograph of the custom-designed gas-tight H-type cell for CO_2RR.

Table S1. Comparison of SnO_2 NPs, CuS NSs and SnO_2/CuS NSs of different ratio for syngas compositions.

Catalysts	Accessible range of syngas ratio (CO/H_2)	FE of syngas ($CO+H_2$) (%)	j_{syngas}[a] (A/g)	TOF of syngas[b] (h^{-1})
SnO_2 NPs	0.07 ~ 0.63	55.5 ~ 98.6	6.3 ~ 21.4	17.68 ~ 60.10
CuS NSs	0.002 ~ 0.38	51.2 ~ 76.9	6.0 ~ 22.5	10.64 ~ 40.10
SnO_2/CuS NSs (1:1)	0.02 ~ 0.25	62.7 ~ 99.9	3.8 ~ 23.4	7.88 ~ 48.84
SnO_2/CuS NSs (1:2)	**0.11 ~ 3.86**	**85.7 ~ 100**	**7.0 ~ 48.0**	**14.02 ~ 96.12**
SnO_2/CuS NSs (1:3)	0.04 ~ 1.7	91 ~ 100	4.3 ~ 39.7	8.12 ~ 74.57
SnO_2 NPs + CuS NSs	0.02 ~ 1.2	80.8 ~ 86.2	4.6 ~ 35.9	9.24 ~ 71.95

[a] j_{Syngas} was defined as the sum of partial current of CO and H_2 per unit mass of catalyst.

[b] Turnover frequency (TOF) of syngas is defined as the mole of syngas ($CO+H_2$) generated per electrocatalytic active site per unit time. Since both SnO_2 NPs and CuS NSs are active for producing CO and H_2, we assumed the electrocatalytic active sites as the moles of both SnO_2 and CuS. And the TOF for syngas was calculated as follows: $\mathrm{TOF} = \frac{j_{syngas} \times \mathrm{A} / NF}{m_{cat} / M_{cat}} \times 3600$, where j_{syngas} is the sum of partial current density for CO and H_2; A is the electrode area, which is $1cm^2$ in this work; N is the number of electron transferred for syngas formation, which is 2 for CO or H_2; F is the Faradaic constant, 96485 $C \cdot mol^{-1}$, m_{cat} is the catalyst mass loading on the electrode, which is 0.4 mg in this work; M_{cat} is the molar mass of catalyst, which is depending on the composition of catalyst.

Table S2. Comparison of aqueous catalysts for different syngas compositions.

Catalysts	Preparation method	Electrolyte	Accessible range of syngas ratio (CO/H_2)	FE of syngas ($CO+H_2$) (%)	Potential range (V *vs.* RHE)	j_{syngas} (mA/mg)	TOF of syngas ($CO+H_2$) (h^{-1})	Ref.
SnO_2/CuS NSs (1:2)	**One-pot wet-chemistry**	**0.1 M $KHCO_3$**	**0.11-3.86**	**85.7-100**	**-0.6~-1.0**	**7.0~48.0**	**14.02~96.12**	**This work**
Co/Au nanostructured electrocatalysts	Two-step Electrodeposition	0.1 M $KHCO_3$	0.43-4	NA	-0.6~-1.0	NA[a]	NA	
Fe/Au nanostructured electrocatalysts	Two-step Electrodeposition	0.1 M $KHCO_3$	0.26-2.78	NA	-0.7~-1.1	NA	NA	*Joule* **2019,** *3*, 257
Ni/Au nanostructured electrocatalysts	Two-step Electrodeposition	0.1 M $KHCO_3$	0.48-10.88	NA	-0.7~-1.1	NA	NA	
$Cu/Ni(OH)_2$ NSs	Template-guided wet-chemistry	0.5 M $NaHCO_3$	0.05-11.5	~100	-0.4~-1.0	8.6@-0.5V (*vs.* RHE)	13@-0.5V (*vs.* RHE)	*Sci. Adv.* **2017,** *3*, e1701069
Polycrystalline Cu foil	Pulsed-bias electrochemical reduction	0.1 M $KHCO_3$	0.03-1.78	100	-1.1	NA	NA	*ACS Catal.* **2016,** *6*, 4739.
Ag NPs	NA	0.5 M $KHCO_3$	0.22-2.33	95	-0.87~ -1.27	3.75@-0.87V (*vs.* RHE)	7.2@-0.87V (*vs.* RHE)	*ACS Energy Lett.* **2016,** *1*, 1149
Ag/g-C_3N_4	Wet-chemistry	0.1 M KH_2PO_4/K_2HPO_4	0.01-0.5	95	-0.75~ -1.3	0.184~1.4	0.31~2.35	*ChemElectroChem* **2016,** *3*, 1497.
Ru(II) polypyridyl carbine complex	Organic chemistry	0.5 M $NaHCO_3$	0.38-2	99	-1.2~ -1.5 (*vs.* NHE)	0.001~0.0019	0.015~0.028	*Energy Environ. Sci.* **2014,** *7*, 4007.
Oxide-derived Au foil	Electrochemical square-wave potential pulse	0.5 M $NaHCO_3$	2.7	89	-0.25	NA	NA	*J. Am. Chem. Soc.* **2012,** *134*, 19969.
CdS_xSe_{1-x} nanorods (x: 0~1)	Solvothermal	0.1 M $KHCO_3$	0.25~4	100	-1.2	64~67.8 @ -1.2V (*vs.* RHE)	182.6~228.5 @ -1.2V (*vs.* RHE)	*Adv. Mater.* **2018,** *30*, 1705872
Au NPs (8 nm)	Surfactant-guided wet-chemistry	0.5 M $KHCO_3$	0.3~9	100	-0.37~ -0.87	0.35~11.1	1.29~40.79	*J. Am. Chem. Soc.* **2013,** *135*, 16833.
Cu-enriched Au nanoneedles	Underpotential deposition	0.5 M $KHCO_3$	0.62-3.33	100	-0.35~ -0.65	NA	NA	*J. Am. Chem. Soc.* **2017,** *139*, 9359.
Pd NPs	NA	0.5 M $NaHCO_3$	~0.25-0.75	~80-90	-0.5~ -1.0	3.19~110	6.33-218.39	*Energy Environ. Sci.* **2017,** *10*, 1180
Co_3O_4-CDots -C_3N_4	High temperature calcination (550 ºC)	0.5 M $KHCO_3$	0.25~14.29	~95	-0.35~ -0.6	~ 10@-0.6V (*vs.* RHE)	NA	*Nat. Commun.* **2017,** *8*, 1828.
Metal-Doped Nitrogenated Carbon	High temperature pyrolysis (900 ºC)	0.1 M $KHCO_3$	~ 1.1 - 5.5	~ 100	-0.5 ~ -0.7	2.8 ~ 11.3	NA	*Angew. Chem. Int. Ed.* **2015,** *54*, 10758
Cu/In_2O_3-0.4 Core/shell NPs	Two-step seed-mediated surfactant-guided wet-chemistry	0.5 M $KHCO_3$	0.67 – 2.5	~ 90-95	-0.4 ~ -0.9	3.09~26.14	10.08~85.32	*ACS Appl. Mater. Interfaces.* **2018,***10*,36996

Nanoporous silver	Two-step chemical dealloying	0.5 M $KHCO_3$	0.04 - 7.56	100	-0.25 ~ -0.5[b]	0.009~0.223	0.017~0.449	*Nat. Commun.* **2014**, *5*, 3242.
Zn dendrite	Electrodeposition	0.5 M $NaHCO_3$	1.75 - 3.95	98-99	-0.9 ~ -1.1	6.29 ~ 17.54	NA	*ACS Catal.* **2015**, *5*, 4586.
Hexagonal Zn	Electrodeposition	0.5 M $KHCO_3$	0.49 – 5.26	100	-0.6 ~ -1.1	NA	NA	*Angew. Chem. Int. Ed.* **2016**, *55*, 9297.
Ni–N–C	High temperature pyrolysis	0.1 M $KHCO_3$	1.13 - 5.67	100	-0.6 ~ -0.85	2.52 ~ 20	0.57~4.53	*Energy Environ. Sci.*, **2019**, *12*, 640.
COF-367-Co	Two-step Solvothermal	0.5 M $KHCO_3$	3.86 @ -0.67 V	100	-0.57~ -0.97	13@-0.67 V (*vs.* RHE)	165 @ -0.67 V	*Science,* **2015**, *349***,** 1208.

[a] NA means not available from the article.

[b] When the potential is more negative than -0.6 V (*vs.* RHE), trace amounts of formate were detected while the FEs of formate are not provided. In order to ensure the data accuracy, potential range is selected from -0.25 to -0.5 V (*vs.* RHE) for calculating related data.

Table S3. Comparison of the ratios of Sn/Cu in different SnO_2/CuS NSs samples obtained from the EDS and XPS results.

Samples	**Sn / Cu (*At %*)**	
	EDS	**XPS**
SnO_2/CuS (1:1)	29.83/70.17	31.06/68.94
SnO_2/CuS (1:2)	21.67/78.33	21.88/78.12
SnO_2/CuS (1:3)	9.38 /90.62	9.52 /90.48

Table S4. Comparison of CO_2RR performance for Cu-Sn based electrocatalysts and other low cost electrocatalysts of high CO selectivity in aqueous.

Catalysts	Preparation method	Electrolyte	Potential range (V *vs.* RHE)	Main product	FE (%)	Partial current densities (mA/cm^2)	Ref.
SnO_2/CuS NSs (1:2)	**One-pot wet-chemistry**	**0.1 M $KHCO_3$**	**-0.6 ~ -1.0**	**CO**	**10 ~ 69**	**0.28 ~ 15.2**	**This Work**
$CuSn_3$ alloy	Co-electrodeposition	0.1 M $KHCO_3$	-0.4 ~ -0.6	Formate	60 ~ 95	31 @ -0.5 V	*Nat. Catal.* **2019,** *2,* 55.
CuO/SnO_2 nanowire	Two-step wet-chemistry and post-calcination	0.5 M $KHCO_3$	-0.7 ~ -1.2	Formate	70 ~ 90	6 ~ 21	*Nano Energy,* **2019**, *59*, 138.
Cu-Sn bimetallic/ rGO	Multi-step electroreduction metal stannate/graphene	0.5 M $NaHCO_3$	-0.8 ~ -1.2	Formate	50 ~ 87.4	4.5 ~ 21.8	*J. Mater. Chem. A*, **2018**, *6*, 7851
CuO/hollow SnO_2 nanoparticle	Two-step wet-chemistry and post-calcination	0.1 M $KHCO_3$	-0.7 ~ -1.0	CO/ Formate	70.1 for CO @ -0.7V, 71.5 for formate@-1.0	1.66 for CO @ -0.7V, 121.6 for formate@-1.0	*Nat. Commun.* **2018,** *9*, 4933.
Bimetallic Cu-Sn	Electrodeposition	0.1 M $KHCO_3$	-0.4 ~ -0.8	CO	82 ~ 90	0.33 ~ 3.1	*ACS Catal.* **2016**, *6*, 2842
CuO/SnO_2 nanowire	Two-step anodization and atomic layer deposition	0.1 M $NaHCO_3$	-0.5 ~ -0.9	CO	78 ~ 90	0.2 ~ 2.6	*Nat. Energy* **2017,** *2*, 17087
Core/Shell Cu/SnO_2-0.8	Two-step seed-mediated wet-chemistry	0.5 M $KHCO_3$	-0.6 ~ -1.0	CO	80 ~ 93	4.3 @ -0.7 V	*J. Am. Chem. Soc.* **2017**, *139*, 4290.
Cu-Sn foam	Electrodeposition	0.1M $KHCO_3$	-0.5 ~ -1.1	CO	70 ~ 94	0.5 ~ 8.2	*Appl. Catal. B: Environ.* **2018**, *236*, 475
Cu/SnO_x(6.2 %)-CNT	One-pot wet-chemistry	0.1 M $KHCO_3$	-0.79 ~ -1.19	CO	68 ~ 89	4 ~ 11.3	*ACS Appl. Mater. Interfaces* **2017**, *9*,28519.
Cu_xO-Sn nanowire	Electroless deposition	0.1 M $KHCO_3$	-0.7 ~ -1.1	CO	44 ~ 82	1.3 ~ 6.7	*J. Mater. Chem. A*, **2016**, *4*, 10710
Cu_2O/Sn	Solvothermal	0.1 M $KHCO_3$	-0.6 ~ -0.8	CO	70 @ -0.6V 80 @ -0.8 V	2.5 @ -0.6V, 20 @ -0.8 V	*ChemSusChem* **2017,** *10*, 1255.
COF-367-Co	Two-step Solvothermal	0.5 M $KHCO_3$	-0.57 ~ -0.97	CO	91 @ -0.67 V	3 @ -0.67 V	*Science,* **2015***, 349***,** 1208.
nanoporous silver	Two-step chemical dealloying	0.5 M $KHCO_3$	-0.4 ~ -0.9	CO	81 ~ 93	2.71 ~ 34.7	*Nat. Commun.* **2014**, *5*, 3242.
Hexagonal Zn	Electrodeposition	0.5 M $KHCO_3$	-0.7 ~ -1.1	CO	64.8 ~ 85.4	2 ~ 20.4	*Angew. Chem. Int. Ed.* **2016**, *55*, 9297.
Zn dendrite	Electrodeposition	0.5 M $NaHCO_3$	-0.9 ~ -1.1	CO	63 ~ 79	4 ~ 14	*ACS Catal.* **2015**, *5*, 4586.
Ni–N–C	High temperature pyrolysis	0.1 M $KHCO_3$	-0.6 ~ -0.85	CO	53 ~ 85	1 ~ 12	*Energy Environ. Sci.,* **2019**, *12*, 640.

Table S5. Zero-pint energy correction (*E*ZPE), entropy contribution (*TS*), and the total free energy correction (*G* − *E*elec) in this work.

Systems	E_{ZPE} **(eV)**	**TS (eV)**	E_{ZPE}**-TS (eV)**
H_2	0.281	0.392	-0.111
H_2O	0.583	0.603	-0.02
CO	0.139	0.560	-0.421
CO_2	0.307	0.595	-0.288
HCOOH	0.804	0.859	-0.055
CO* on CuS (001)	0.491	0.390	0.101
COOH* on CuS (001)	0.659	0.436	0.223
OCHO* on CuS (001)	0.677	0.429	0.248
CO* on SnO_2 (110)	0.326	0.267	0.059
COOH* on SnO_2 (110)	0.589	0.304	0.285
OCHO* on SnO_2 (110)	0.594	0.311	0.283
CO* on SnO_2 (110) / CuS (001)	0.767	0.602	0.165
COOH* on SnO_2 (110) / CuS (001)	0.886	0.491	0.395
OCHO* on SnO_2 (110) / CuS (001)	0.892	0.499	0.393

References

1 M. Bajdich, M. García-Mota, A. Vojvodic, J. K. Nørskov and A. T. Bell, *J. Am. Chem. Soc.*, 2013, **135**, 13521-13530.

2 B. Hammer, L. B. Hansen and J. K. Nørskov, *Phys. Rev. B*, 1999, **59**, 7413-7421.

3 N. T. K. Thanh, N. Maclean and S. Mahiddine, *Chem. Rev.*, 2014, **114**, 7610-7630.

4 Y. Du, Z. Yin, J. Zhu, X. Huang, X.-J. Wu, Z. Zeng, Q. Yan and H. Zhang, *Nat. Commun.*, 2012, **3**, 1177.

5 S. Guo, S. Zhao, X. Wu, H. Li, Y. Zhou, C. Zhu, N. Yang, X. Jiang, J. Gao, L. Bai, Y. Liu, Y. Lifshitz, S.-T. Lee and Z. Kang, *Nat. Commun.*, 2017, **8**, 1828.

6 J. Zuo, C. Xu, X. Liu, C. Wang, C. Wang, Y. Hu and Y. Qian, *J. Appl. Phys.*, 1994, **75**, 1835-1836.

7 W. Zhang, Q. Qin, L. Dai, R. Qin, X. Zhao, X. Chen, D. Ou, J. Chen, T. T. Chuong, B. Wu and N. Zheng, *Angew. Chem. Int. Ed.*, 2018, **57**, 9475-9479.